Technical Report

Team 02

UVigo Aerotech

Air Cargo Challenge 2024

ADDI

30.04.2024

Contents

Tables

Figures

1.- Introduction

UVigo Aerotech is a student project aimed at designing, manufacturing, and constructing model aircraft with the goal of participating in national and international university competitions related to aero design. In addition to being the only team from Galicia set to participate in these competitions, this year marks the beginning of a new initiative within the team: **UVigo Aerotech: Research & Development**. As its name suggests, this initiative focuses on the research and development of technological solutions in diverse fields such as structural monitoring, coastal and forest surveillance, as well as assistance in search and rescue operations.

This past season (2022-2023) represented the team's 4th season, which has been serving students from degrees such as Aerospace Engineering, Tourism, Computer Engineering, Law, and Business Administration for more than 3 years to be part of a real engineering project.

The project was launched in January 2020 at the suggestion of one of the professors from the School of Aeronautical and Space Engineering, Guillermo Rey, who proposed creating a model aircraft team aimed at participating in inter-university competitions, operating in a similar manner to other projects at the University of Vigo like UVigo Motorsport. After two years, in July 2022, **UVigo Aerotech** participated in the **Air Cargo Challenge 2022** with its first manufactured aircraft, **CORV-0**, which was entirely developed by students from the University of Vigo.

Figure 1. UVigo Aerotech in season 2021-2022

2.- Project Management

2.1. Internal Team Structure

This season has already become the one with the most members on the team, totalling 44 members. This figure also highlights the interest of the university community in our project, now involving not only undergraduate engineering students but also master's students such as those in Aeronautical Engineering. Moreover, the addition of a concurrent engineering project like **UVigo Aerotech: Research & Development** necessitates a restructuring of our internal organization.

While the roles of president, treasurer, and secretary remain unchanged, the internal structure of the project aimed at the 'Air Cargo Challenge 2024' competition has been simplified. Now, this part of the team consists of a Team Leader, a Technical Leader, and 4 department heads instead of 5 as in the previous season. Thus, the Executive Board and its roles remain virtually unchanged, but the Technical Departments of the team are now:

- Aerodynamics Department.
- Structures and Dynamics Department.
- Propulsion and Control Department.
- Organization and Marketing Department.

On the other hand, the R&D (Research & Development) project is directly supervised by the Team Leader, while it is divided into 3 sub-departments:

- Design Department.
- Autonomous Control and Recognition Department.
- Solar Propulsion Department.

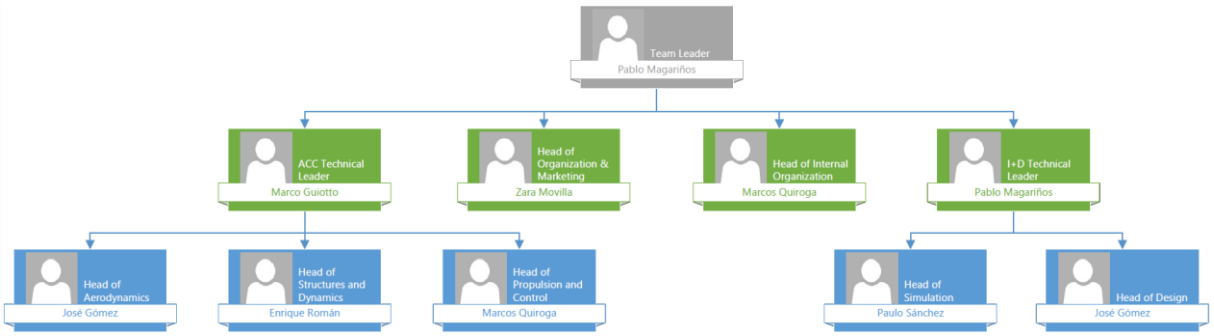

Figure 2. Team Organization

The following chart exposes how we have planned this season from August until July:

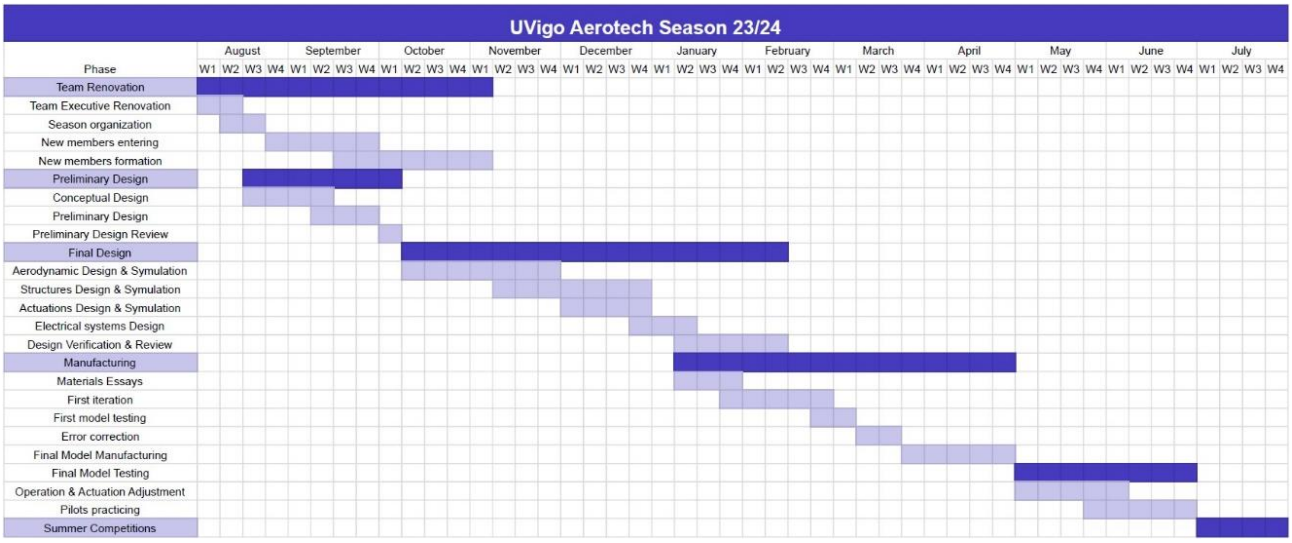

Figure 3. Gantt chart about our time organization

2.2. Sponsors

Like most university projects, UVigo Aerotech does not have its own funding. Therefore, through the support of our sponsors, we are able to design and manufacture our model aircraft, as well as participate in various competitions and events. Our team has a sponsorship plan that categorizes sponsors into different levels (Alpha, Beta, Gamma, Delta) based on the agreement reached.

In our case, sponsors provide not only financial assistance but also their services, workspace, and support throughout our various projects. As a form of appreciation and gratitude, our sponsors' logos are prominently displayed on both our model aircraft and the team's polo shirts.

Figure 4. Our sponsors

3.- Aerodynamic Design and Aircraft Optimization

3.1. Propeller

A wide range of options were evaluated to achieve the optimal set of working conditions in the propeller, utilizing the resources available on the APC Propellers website. Firstly, every .dat file underwent initial processing by conversion into an Excel format. Subsequently, a MATLAB calculated the most suitable information for the following analysis. For instance, the adjustment of amperage serves as an illustration of this procedure.

Our own selection criteria were employed among the entire array of propellers, focused mainly on the flight distance, flight efficiency and maximum load capacity. This approach was based on a points-awarded system, with a maximum of 1000 points for each measure. A mean average was then computed across all data. Afterwards, potential penalties for exceeding the amperage limits were deducted from each value, to ensure compliance with the competition regulations.

$$\text{Sum of points} = \frac{\text{Distance} + \text{Efficiency} + \text{Load}}{3} - \text{Penalties}$$

By conducting three distinct tests, slightly changing the initial conditions, targeting maximizing load capacity, optimizing efficiency, and applying personal criteria, the classification of propellers was established based on overall performance. Consequently, from the top-performing groups across these tests and considering the exclusion of a duct piece due to structural constraints, the APC Speed E 10x6 propeller was chosen, as its performance was deemed the most suitable for achieving our objectives.

With the selection of this propeller as the focal point of further investigation, a performance curve was defined following two different factors: a theoretical mathematical model and the data provided by the eCalc software tool. Initial conditions were configured with a medium power level and ESC synchronous speed. Initially, a notable disparity was noted between the numerical values obtained in eCalc and their substantially lower theoretical counterparts. As a result, a decision was made to increase both the power supplied by the battery and the ESC. This adjustment drew the sets of values closer to each other, achieving the desired convergence.

These modifications are shown in the graph below, which represents the flight speed, on the horizontal axis, versus the thrust generated by the propeller, on the vertical axis. Theoretical values are represented in orange, while values obtained from eCalc are depicted in blue, for medium power and speed, and in green, for the higher ones.

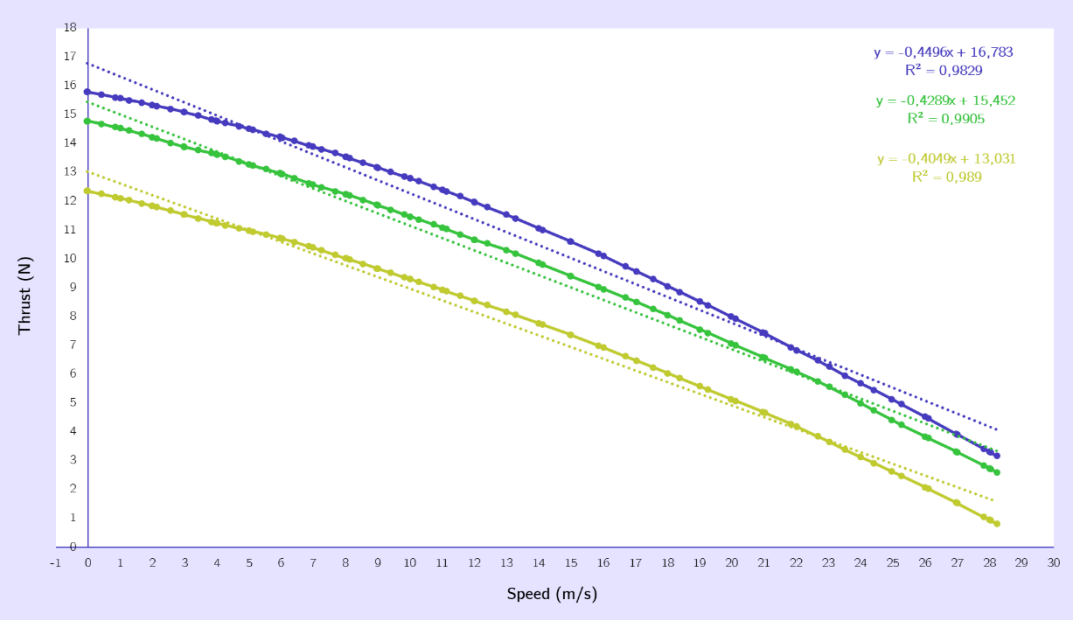

Figure 5. Flight speed VS thrust

As for the obtained values of electrical and mechanical power, efficiency, angular velocity, and torque, they are shown in the table displayed below.

	Theoretical	Medium Conditions	Higher Conditions
Electrical Power (W)	310	206	267
Mechanical Power (W)	239	173	227
Efficiency (%)	77	84	85
Angular Velocity (rpm)	9786	8747	9570
Torque (Nm)	0.23	0.19	0.23

Table 1. Values of electrical and mechanical power, efficiency, angular velocity, and torque

The theoretical values shown in this table have been obtained by calculating the mean average from a discrete sample, encompassing the entire range of functional velocities for the propeller.

It can be seen that, except for the electrical power and, consequently, efficiency, the theoretical and eCalc-obtained values for each parameter are closely aligned. The notable disparity in electrical power and efficiency could be attributed to the absence of consideration for ESC in the mathematical model. Given this discrepancy, it can be said that the eCalc-driven results are sufficiently reliable.

3.2. Preliminary Design

3.2.1. Initial Parameters

To obtain the starting parameters for the aerodynamic design, an analysis of the **Thrust-to-Weight ratio** was performed for the fixed propulsion configuration. The results are presented in the following table:

$C_{L,\ max}$	C_{Lg}	$C_{D,\ min}$	C_{D0}	C_{Dg}	Mass
1.6	1.2	0.016	0.014	0.207	3.5 (kg)

Table 2. Initial Parameters

Additionally, a maximum wing area of 0.4402 (m^2) is calculated, resulting in a minimum (W/S) load factor of 77.9986 (N/m^2). The following distribution of (T/W) relative to speed is obtained:

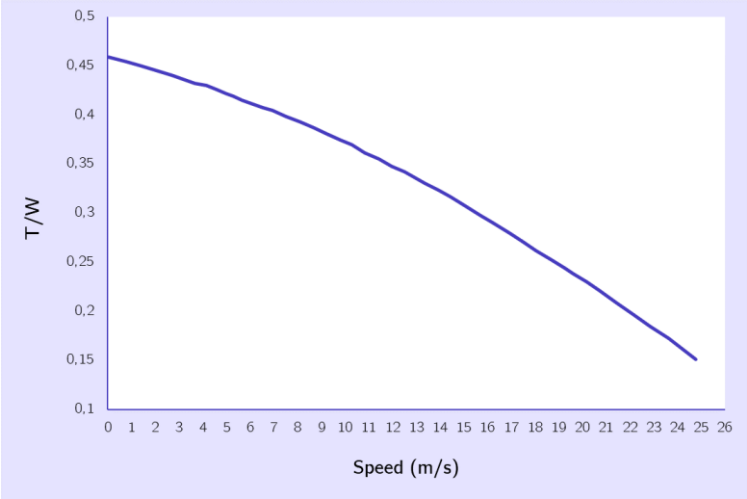

Figure 6. Graph of T/W distribution VS speed

3.2.2. Wing Loading

A wing loading analysis was conducted for the following flight scenarios:

- Take-off.
- Climb/Glide.
- Cruise.
- Sustained Turn.
- Stall Entry.
- Landing.

From this analysis, the following graphical results were attained, along with the conclusions reflected below:

Figure 7. Wing Loading Calculation Results

In order to meet all the wing loading requirements and achieve conditions with reasonable stall speeds by applying a safety factor, a value around **100 (N/m^2)** would be appropriate, in a **$C_{L,\,max}$ of 1.28 for C_L=1, and a $C_{L,\,max}$ of 0.769 for C_L = 0.6.**

3.3. Fuselage Design

3.3.1 Design and Geometry

For the fuselage design, an initial analysis was executed on the components it should accommodate, along with the payload, to approximate a distribution based on the dimensions and weights of each element. Considering the initial goal of placing the CG between $\frac{1}{4}$ and $\frac{1}{3}$ of the wing chord, masses will be avoided at the fuselage extremities.

With these initial conditions, combined with the adaptation to the propulsion configuration featuring the rear-mounted engine, a fuselage was crafted with a sleekly contoured nose, considering the payload dimensions. The aft section was similarly smoothed continuously to the trailing edge to optimize the cleanest possible airflow for the propeller.

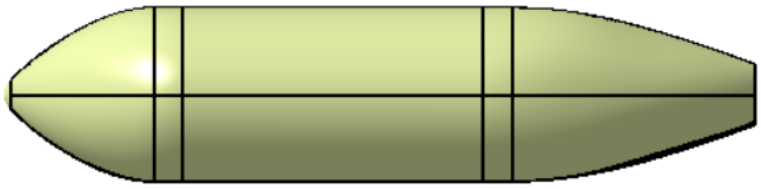

Figure 8. Side view of the 3D fuselage design

The geometry would have the following characteristics:

- Maximum dimensions (length x width x height): 525x240x120 (mm)
- Frontal surface area: 0.024807 (m^2)
- Total fuselage volume: 0.009807 (m^3)

3.4. Wing Design

The wing design was carried out under the following criteria:

- Maximizing efficiency and adapting performance to the competition scoring system.
- Maximizing aircraft maneuverability.

3.4.1. Airfoil

The airfoil design and selection process were performed using the software **xflr5**. A significant portion of the study involves modifying existing profiles in our own database, examining potential improvements in their properties, more favourable to the initial design parameters. From among all the airfoil evaluated, the one that provides the best results in terms of efficiency and performance for our case, has been selected and shown in the next image:

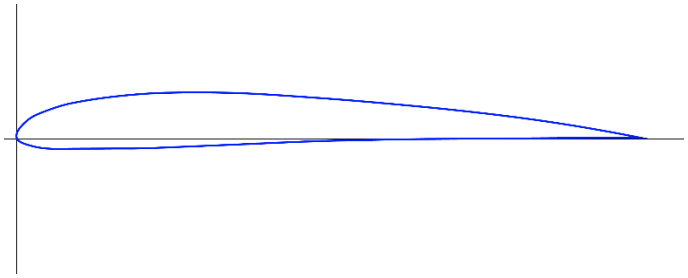

Figure 9. Airfoil displayed in the wing

3.4.2.Geometry

For the geometry of the wing, a variety of wing planform configurations were explored. Among them, some have been studied in different setups using **xflr5**. The configuration that best met the design requirements and yielded the most efficient results was ultimately selected and is displayed in the image below:

Figure 10. Wing planform geometry

As it can be seen, we have designed a configuration with a straight first section, and a second trapezoidal section, with a constant leading-edge sweep.

The main features of this wing are:

- Wingspan (half-wing): 0.91 (m)
- Root Chord: 0.23 (m)
- Mean Aerodynamic Chord: 0.21 (m)
- Aspect Ratio: 9.10
- Taper Ratio: 0.48
- Wing Area (A_w): 0.36 (m^2)

3.4.3. Wingtip (Winglet Design)

To minimize the drag generated by wingtip vortices, the implementation of a winglet is studied, along with various possible configurations to manufacture it. The choice made is based solely on the criteria of enhancing the aerodynamic efficiency of the model, leading us to determine that a raked winglet type offers the optimal configuration.

3.5. Design of the Empennage

Considering the engine placement, the tail design is initially set with an inverted V configuration to mitigate the effects of propeller wake. This configuration aims to minimize induced rotation, thereby safeguarding the aircraft's stability.

3.5.1. Airfoil

Based on the tail configuration, the decision is made to use a symmetrical airfoil profile. A study is conducted with various profiles, and the **NACA 0008** is determined to be the optimal choice. Additionally, this profile offers sufficient space to accommodate the control surface mechanism without compromising aerodynamics.

3.5.2. Dimensioning and Design

For the empennage design, an initial sizing is conducted for a conventional configuration, which will then be adjusted according to the vertical and horizontal projections. The entire process is based on documents from the **Polytechnic University of Madrid**, with conversion using documentation from the **Technical University of Munich**.

An estimation of the center of gravity (CG) is calculated for a position at one-quarter chord $\left(\frac{c}{4}\right)$. This is achieved by applying the following formulas for horizontal (h) and vertical (v) sizing, respectively:

$$A_h = \frac{V_h \cdot A_w \cdot MAC}{l_h}$$

$$Width_h = \sqrt{\frac{A_h}{3.5}}$$

$$Lenght_h = Width_h \cdot 3.5$$

$$A_v = \frac{V_v \cdot A_w \cdot b}{l_h}$$

$$Width_v = \sqrt{\frac{A_v}{3.5}}$$

$$Lenght_v = Width_v \cdot 3.5$$

Through those equations, the following results are obtained:

- Horizontal stabilizer area (A_h): 0.204 (m^2)
- Vertical stabilizer area (A_v): 0.126 (m^2)
- Horizontal stabilizer width ($Width_h$): 0.241 (m)
- Vertical stabilizer width ($Width_v$): 0.189 (m)
- Horizontal stabilizer length ($Length_h$): 0.844 (m)
- Vertical stabilizer length ($Length_v$): 0.663 (m)

Finally, the angle of inclination that the empennage will have is calculated using the following formula: $\theta = \tan^{-1}\left(\sqrt{\frac{A_h}{A_v}}\right) = 38.16^{\circ}$

After conducting stability simulations in **xflr5**, a final design of the empennage is established, featuring a total projected area of 0.15 (m^2) in plan, a Mean Aerodynamic Chord (MAC) of 0.19 (m), and a projected span of 0.63 (m). The geometry is configured with a trapezoidal shape, with a chord that progressively increases from the root to the empennage socket, ensuring a larger surface area exposed to clean airflow.

3.6. Control Surfaces

3.6.1. Flaps

The implementation of different types of flaps is examined considering the aircraft configuration, along with the possibility of omitting them altogether. After analyzing various configurations in **xflr5**, a conventional flap configuration with deflection of up to 20º in 10º intervals was selected. This decision aligns with the design criteria observed in other aircraft with trapezoidal wings, setting a flap area equivalent to 15% of the semi-wing area.

By incorporating this device, a maximum increase of 35% in lift is achieved during the take-off phase, under conditions of 12 to 15 (m/s) and an angle of attack (AoA) of 5º. The quantitative results are as follows:

- Take-off (12 (m/s) flaps 20, AoA 5º): 35 (N)
- Take-off (15 (m/s) flaps 20, AoA 5º): 41 (N)
- Climb/Approach (15 (m/s) without flaps, AoA 10º): 44 (N)
- Climb/Approach (15 (m/s) flaps 20, AoA 10º): 56 (N)

Along with the propulsion data, the following values are set for the final configuration that will be operated under normal conditions:

- $V_{Take\text{-}off}$ = 15 (m/s)
- $C_{LTake\text{-}off}$ = 0.97
- Take-off Distance = 30 (m)
- AoA = 5º
- Deflection = 20º

3.6.2. Ailerons/Spoilers

The sizing of the ailerons is carried out under the following criteria:

- The surface of each aileron will be ~10% of the surface of each semi-wing.
- The aileron chord will be around 25% of the wing chord.
- The maximum length will be 50% of the half wing.

Taking this into consideration, the ailerons are dimensioned, and an analysis of their behaviour is conducted. The final design of the ailerons has a surface area of 0.016 (m^2) each, featuring symmetrical deflection at a 1:1 ratio. The results from an examination of warping moments confirm, with maximum deflections set at 25º in each direction.

3.6.3. Stabilizers

The sizing of these surfaces is conducted using analytical methods, followed by verification using Computational Fluid Dynamics (CFD). The neutral point is calculated, along with the minimum deflection, thus determining the CG limit for aircraft operation. The following results are obtained once the design has been verified:

- Control surface area: ~75% of total empennage area.
- Maximum deflection (critical): [+30º, -30º]
- Deflections in flight: [+20º, -20º]

3.7. Stability Analysis

For the stability analysis, the following flight mechanics formulas developed in **MATLAB** are utilized, incorporating coefficients previously derived from results of CFD simulations on the various deflections of the control surfaces and high-lift devices:

$$C_{mA}=C_{m0}+C_{m\alpha}\cdot\alpha_{wb}+C_{m\delta_e}\cdot\delta_e$$

$$C_L=C_{L0}+C_{L\beta}\cdot\beta+C_{L\delta_a}\cdot\delta_a+C_{L\delta_r}\cdot\delta_r$$

$$C_n= C_{n0}+C_{n\beta}\cdot\beta+C_{n\delta_a}\cdot\delta_a + C_{n\delta_r}\cdot\delta_r$$

3.7.1. Center of Gravity Analysis

A calculation of the Center of Gravity is conducted by considering the distributions of the components and treating them as point masses. This is modelled in **xflr5**, and the neutral point of the aircraft is extensively calculated for both empty and maximum payload scenarios. The resulting positions of the Center of Gravity concerning the chord at the root are as follows:

- $\frac{x}{c}$ **= 0.4565 in max. load** at 105 (mm) from the leading edge.
- $\frac{x}{c}$ **= 0.6522 in empty** at 150 (mm) from the leading edge.

3.7.2. xflr5 Analysis

The results obtained in **MATLAB** are compared with a stability analysis in **xflr5**.

The extreme scenarios for aircraft in empty and maximum load configurations are discussed:

- In the absence of external influences, a $C_{mA} = 0$ is achieved at an angle of attack of 1.35º and a speed of 17.5 (m/s), corresponding to cruising without control surface deflections. **The C_m versus Alpha (α) slope exhibits a negative trend**.
- In the maximum load configuration, a $C_{mA} = 0$ is achieved at an angle of attack of -0.37º and a speed of 24.4 (m/s), also corresponding to cruising without control surface deflections. **The C_m versus Alpha (α) slope maintains a negative trend**.

The analysis confirms that in both extreme cases, the aircraft exhibits horizontal stability, as it can return to its longitudinal equilibrium position after a disturbance, as evidenced by the negative slope of C_m – Alpha. This is also proven by calculating the position of the neutral point of our aircraft in both empty and MTOW scenarios, which gives us values for the stability margin between 0.33 and 0.54 respectively.

Furthermore, the condition of lateral stability is also verified, which is crucial, especially during crosswind conditions. This is attributed to the negative slope of the rolling moment versus C_L and the positive slope of the yaw moments versus C_n.

3.7.3. CFD Analysis

One of the primary analyses conducted using Computational Fluid Dynamics (CFD) is the assessment against perpendicular crosswind gusts of 10 (m/s), a critical condition for the competition. This evaluation reveals a negative moment on the Z-axis of the aircraft, leading to an increase in the glide angle. To address this situation, the stabilizers are utilized to maintain the desired course. This analysis is performed for both climbing and cruising conditions.

3.8. Final Aircraft Parameters

Speeds	Cruising speed	25 (m/s)
	Max. speed	27 (m/s)
	Stall speed	11 (m/s)
	Take-off speed	15 (m/s)
Aircraft Performance	Max. angle of rotation	56.3º
	Load factor	1.5
	Climb speed	1.8 (m/s)
	Total drag during cruise	4.5 (N)
	Max. efficiency	14.6
Wing (cruise)	C_L	0.2916
	C_D	0.0205

Figure 11. Final Aircraft Parameters

4.- Structural Design and Manufacturing

4.1. Wing Structural Design

Due to dimensional constraints, each half-wing comprises two parts: a central rectangular section and a trapezoidal section where the wingtip is affixed.

4.1.1. Skin

Crucial for structural integrity, the skin must be chosen meticulously. Optimal results were achieved using two layers of twill [0,0], with a total thickness of 0.36 (mm). This laminate provides the necessary mechanical properties for the carbon fiber to withstand aerodynamic forces and transfer them to the ribs effectively. Later in the MEF analysis a laminate of three layers of twill [0,45,0] was also studied for the wood internal structure.

The skin features surface variations to facilitate attachment of the empennage tube to the wing and is divided into sections corresponding to the half-wing components and the upper and lower camber surfaces.

4.1.2. Internal structure

When designing the internal structure of the wing, different limiting factors were considered, setting the parameters for the rest of the design.

Each half-wing consists of twelve ribs, with seven located in the first section and five in the second. Ribs 1 to 4 and 10 are trimmed as they align with the control surfaces (flap and aileron respectively). Ribs 7 and 8 are joined together to streamline the connection between the two parts of the half-wing. These ribs are strategically positioned to enhance rigidity in critical areas, including the root rib, the interconnecting ribs, and those adjacent to the control surfaces.

Each half-wing also consists of three spars, two in the first section and one in the second. Aside from enhancing rigidity and stability, the spars in the first part are also configured to function as connections to the empennage tube.

To join the two parts of the half-wing, two rods have been incorporated to the second part: one up to the final rib, which also enhances the rigidity and stability of this segment, and the other up to the ninth rib. These rods are inserted into two tubes in the first section of the half-wing, spanning from the sixth to the seventh rib. Furthermore, to reinforce the joint, additional pieces have been included to secure and, simultaneously, facilitate disassembly by pulling both parts in opposite directions.

Finally, two tubes have been installed at the base of the half-wing, up to the second rib, to establish a connection between the wing and the fuselage.

In terms of the materials, our initial approach involves creating sandwich panels using carbon fiber and foam cores, from which we will fabricate both the ribs and spars. However, since this method is untested for us, we will also prepare ribs and spars from wood as an alternative

option. On the other hand, the tubes will be made of carbon fiber and sourced in the required diameters.

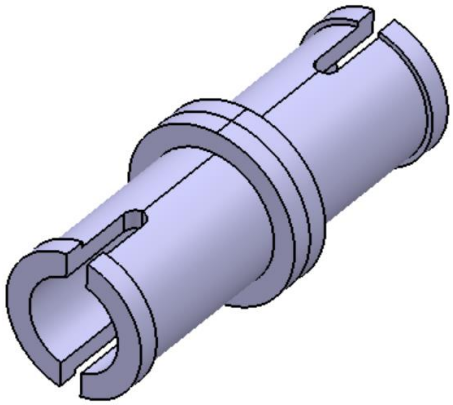

Figure 13. Pin

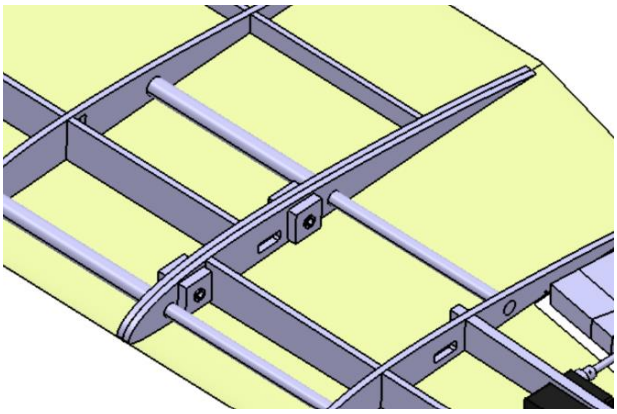

Figure 13. Wing union

4.1.3. Flap, aileron and wingtip

The flap, aileron and wingtip consist of the same skin as the rest of the wing. The entire surface of each part of the half-wing is laminated uniformly, after which the control surfaces are cut out. Similarly, the wingtip shares the same skin as the second part of the half-wing, as it is affixed to the wingtip.

The flap, aileron and wingtip are machined from Divinycell H45 foam and then glued to the skins. Additionally, in the case of the wingtip, it will be attached to the last rib of each half-wing.

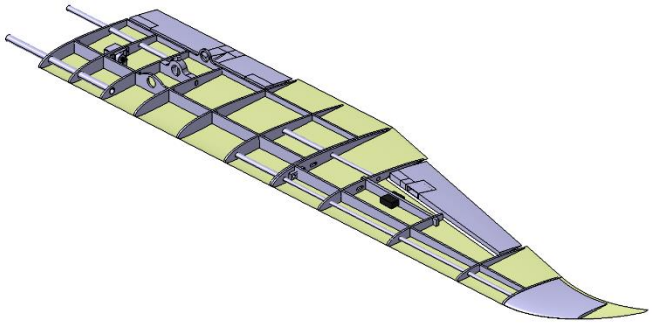

Figure 14. Internal structure of the wing

4.2. Fuselage's Structural Design

The fuselage's design is primarily composed of two elements found in most airframes, frames, and stringers along with ribs and tubes.

4.2.1. Frames

Their primary structural role, alongside the wing skin, is to impart torsional rigidity to the framework. Additionally, they aid in sculpting the aircraft's form, with specific components

serving as foundational support for features like the landing gear or cargo bay. In the aircraft we have introduced 8 frames. The second, third, and fourth frames feature open tops to ease access to the cargo bay. Notches are incorporated into the third, fourth, and fifth frames to accommodate the payload tray. Serving as a bedplate, the eighth frame adds structural support. Furthermore, we've opted to omit a frame in the telemetry zone, as it didn't affect the airframe's structural stability and posed challenges due to element density in the area.

4.2.2. Stringer

Their purpose is to withstand bending forces along the transverse axis. In our aircraft, there are two stringer arrangements: upper and lower. For the lower section, we decided to introduce 5 radial stringers. Unfortunately, due to the complex layout required for the upper part, particularly concerning the aircraft's geometry, telemetry, and cargo bay access window, reinforcing the stringer placement posed a challenge. To address this, we decided to incorporate one vertical stringer centered on the body's axis, from the eighth frame to the sixth. Subsequently, we positioned the remaining two vertical stringers laterally, extending from the seventh to the fourth frame.

4.2.3. Ribs

One of the characteristics of our aircraft model is the smooth transition between the fuselage and the wings. Due to this, it is necessary to install ribs in our fuselage. In our case, we placed a pair on each side. The external ribs are positioned at the wing attachment points, with the objective of covering the main body and reinforcing that region against significant stress.

4.2.4. Tubes

Two tubes traverse the fuselage from one side to the other, serving as the mounting points for the wings. These tubes align with the apertures in the ribs and the two lateral vertical stringers, firmly affixed in place with resin to ensure structural integrity.

Frames, stringers, and ribs are interlocked via specially designed notches, ensuring a snug fit, and then bonded together using adhesive, for example Crestabond, to add strength and stability. Likewise, adhesive is used to bond the fuselage itself with the carbon skin of the aircraft. In the case of the fuselage's frames and stringer we have the same options for the materials as for the wing

Our cargo bay consists of a hexagonal tray constructed from 3 (mm) plywood. It contains 7 holes intended for transporting the payload, which will be secured within frames. The design was specifically engineered to enable the tray to move along the plane's longitudinal axis. This functionality facilitates convenient loading and unloading of the payload, as well as the ability to position it optimally for flight.

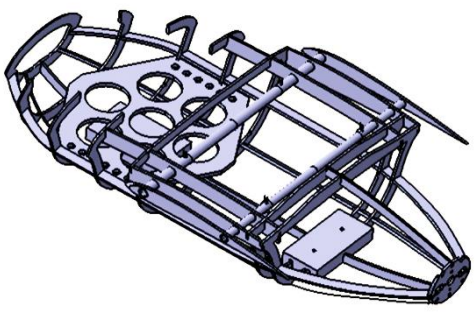

Figure 15. Internal structure of the fuselage

4.3. FEM verification

A finite element simulation tool has been employed to verify the aircraft's structural integrity. Given the complexity of measuring in-flight deflections such that we may correlate the FEM results with reality, we instead opted for a principal simulation that consists in lifting the airplane by its wingtips. This static test ensures the aircraft's airworthiness before any flight operations commence.

The methodology for constructing the aircraft, which utilizes composite materials, involves a preprocessing plugin (**ANSYS ACP**) to define the laminates and their materials.

The aerodynamic skins are constructed using twill SE75 and cured in an autoclave. For the sandwich structure, a PET foam core and unidirectional carbon prepregs with an epoxy Cycom 977-2 matrix are employed.

Directional mechanical properties of the different studied laminates are as follows:

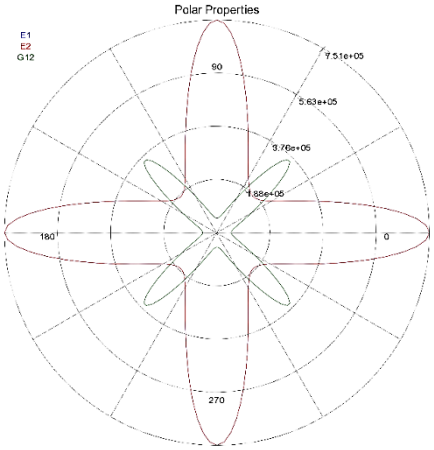

Figure 16. Stackup Twill Cloth 0 0

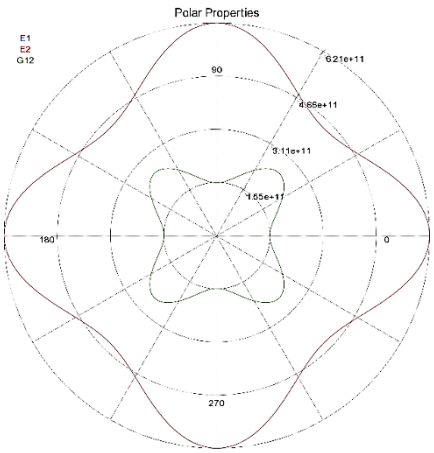

Figure 18. Stackup Twill Cloth 0 45 0

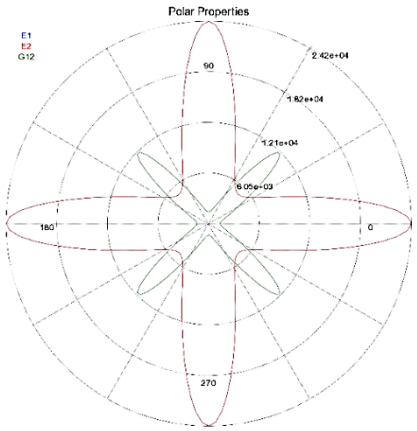

Figure 18. Stackup Twill Sandwich 0 90 Core 90 0

The simulations have been the primary source of information for the structure's iterative design.

At first, the simulation focused on the wing structure of the first section with an internal sandwich configuration. The results from the structural analysis after the static test were favourable, with the most stressed section being the socket area, particularly due to the stress concentrator induced by the tail tube joint. Maintaining a factor of safety higher than 1.5 has consistently been the objective, especially considering that the first section experiences the highest demands from both the wing's aerodynamic bending moment and the torque induced by the empennage.

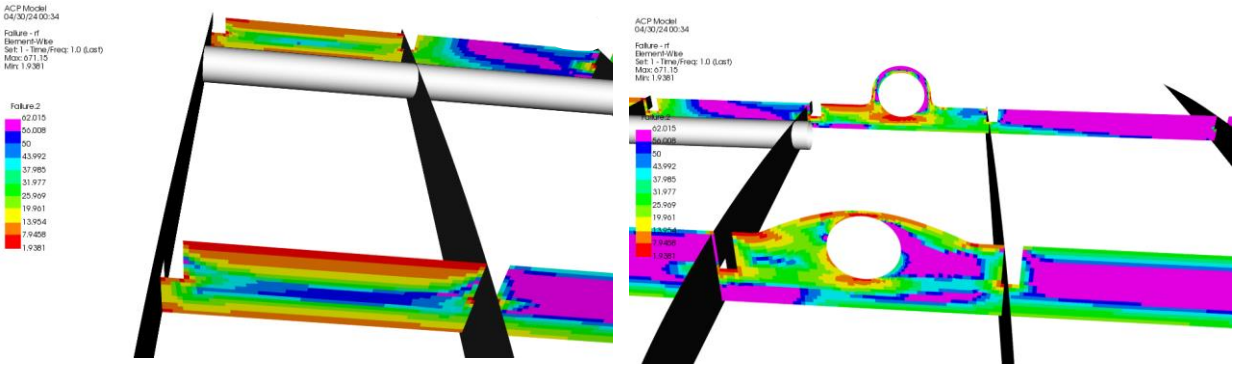

Figure 19. Results from the structural analysis after the static test

One of the studies employed to select the number of ribs as well as their spacing was the wing skin buckling study, whose results showed that the first buckling mode occurs out of the aircraft's flight envelope.

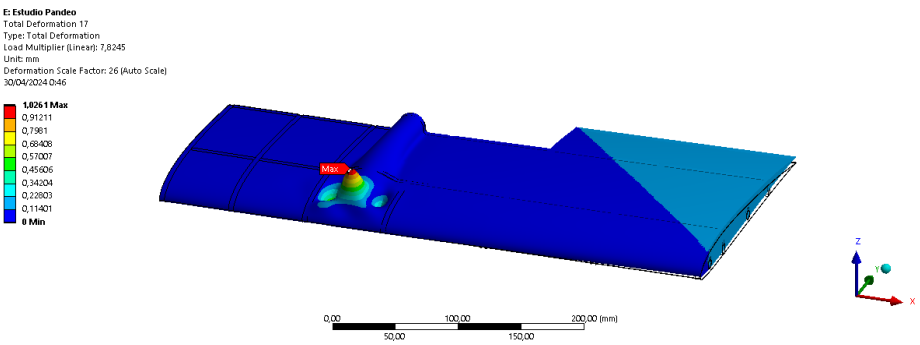

Figure 20. Wing skin buckling study

The total bending deflection in the static test is estimated to be approximately 0.4% of the total span.

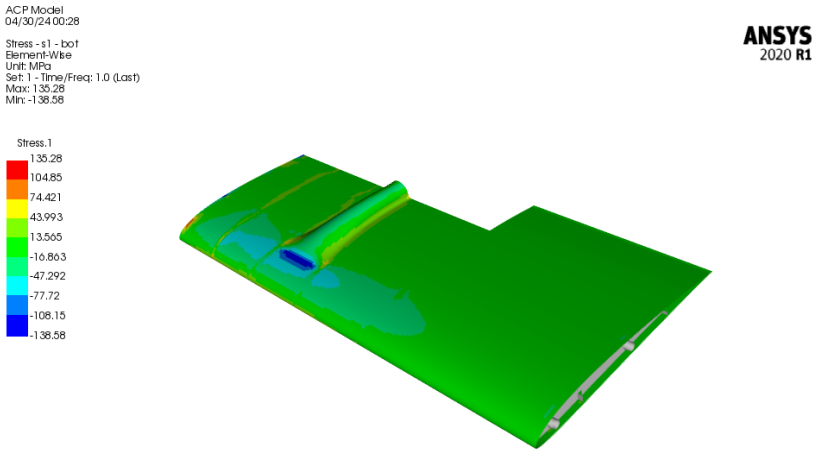

Figure 21. Total bending principal stress in the static test

Applying the same methodology, simulations were conducted for the other two wing structures, namely the internal wood and aluminum structures, yielding the following results:

Structure type	Deflection (mm)	Structural weight per wing (kg)	Minimum Safety Factor
2 Twill 0 0 Layers Sandwich Internal Structure	11.16	0.362	1.51
2 Twill 0 0 Layers Aluminum Internal Structure	4.53	0.612	5.1
3 Twill 0 45 0 Layers Pinewood Internal Structure	9.47	0.492	2.45
3 Twill 0 45 0 Layers Plywood Internal Structure	9.46	0.481	2.92

Table 3. Comparison of the results with different materials

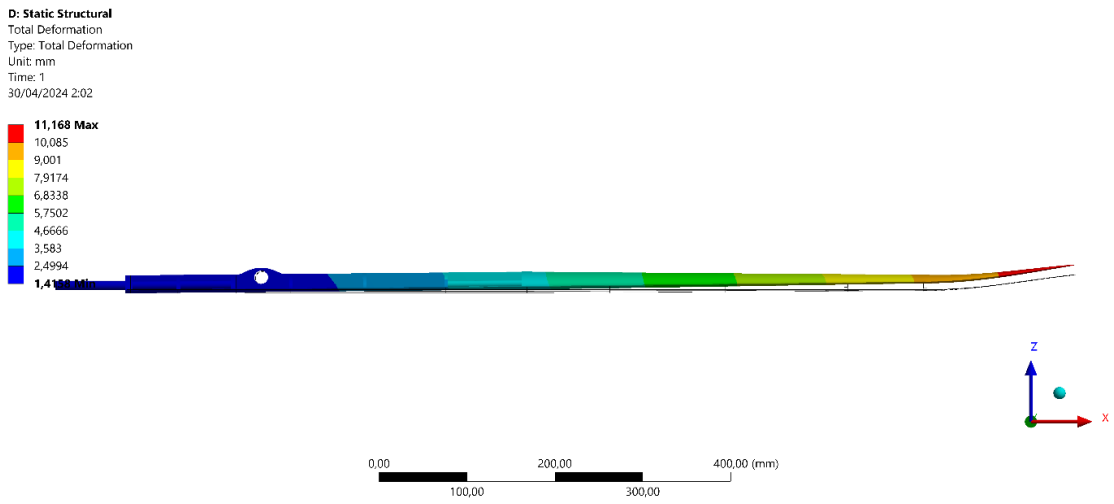

Figure 22. Deformation of the wing

In addition, the torsional stiffness of the structure was tested under diverse loads applied to the tail of the aircraft, demonstrating favourable responses to the stresses.

It is important to note that, as we have seen in the polar graphics of the properties of each laminate, that laminates with layers at 0º are sufficient for the internal structures made from carbon fiber and aluminum since the fibers are aligned with the main directions of stress. Knowing this, and understanding the lower structural properties of wood, especially plywood, an intermediate layer at 45º adds the torsional stiffness needed to ensure that the whole structure behaves the same way as the other structures, and still saves close to 0.25 (kg) of weight from the wings.

Regarding the fuselage verification, the fitting was the primary concern. The structure underwent tests to withstand loads equivalent to a critical force of 10 (kg) applied to the wingtip. The results were optimal, achieving a safety factor close to 1 for both skin and core failures. It's worth noting that the wing is designed to provide less than half of the lift.

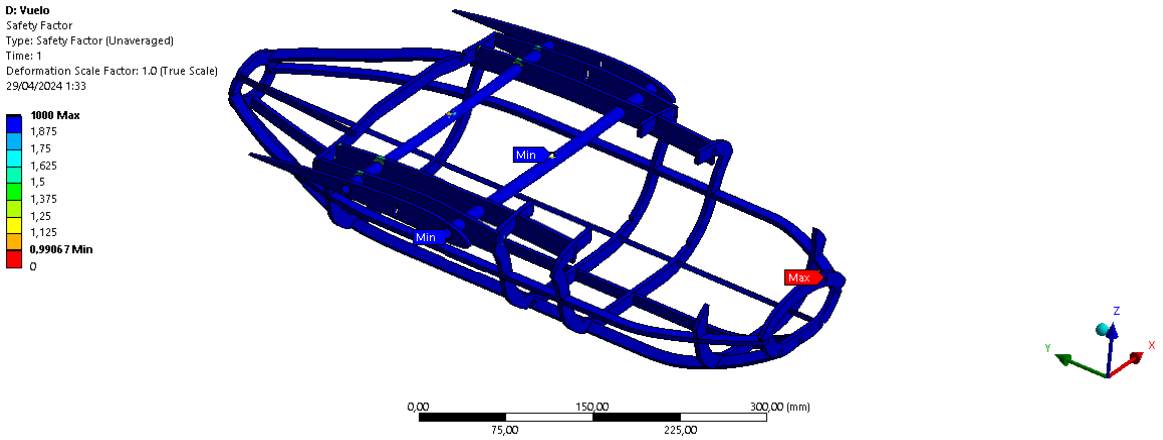

Figure 23. Fuselage wingtip bending simulation results

4.4. Fixations and Joints

In terms of joints, we have chosen varied solutions based on the specific zone.

For the fuselage's wing socket, the laterally inserted tubes from each semi-wing are secured with R-shaped pins/clips, enabling quick and safe manipulation without compromising weight. This joint is primarily subjected to the wing's gliding forces during turns.

To connect the empennage support tubes to the wing, a 3D-printed piece was designed and embedded, then secured to the adjacent ribs, tailored to the zone's geometry. A pin passes through the tube, support, and wing's skins for fixation.

Similarly, the empennage joint, including the tubes and the two control surfaces, utilizes 3D-printed pieces fixed with pins.

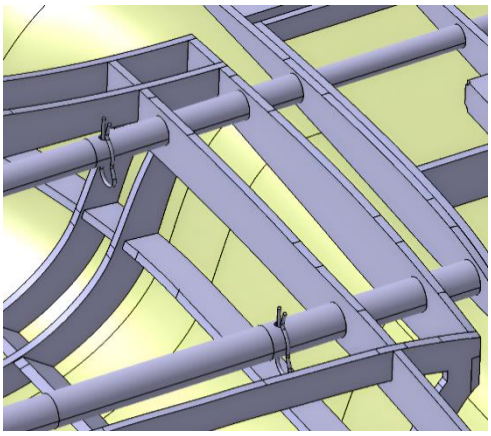

Figure 25. Wing fuselage lock

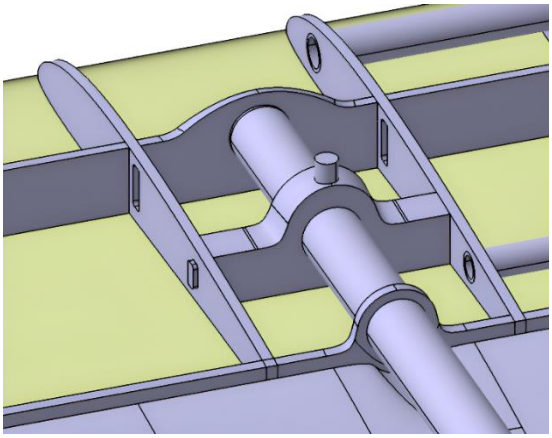

Figure 24. Wing empennage lock

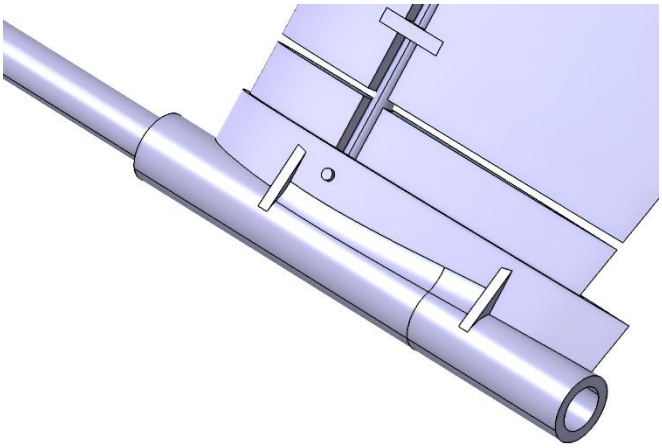

Figure 26. Empennage lock

4.5. Carbon Fiber Pieces

The external surfaces of our drone are made of prepreg carbon fiber. In this way, our team has been able to learn one of the most used manufacturing processes in the aeronautical industry.

Concerning the materials, aluminum has been chosen for the molds due to its favourable characteristics such as density, availability, and ease of surface finishing. Steel was ruled out due to its weight and susceptibility to oxidation. Wood or foam molds were also discarded because they are incompatible with the autoclave cure cycle, as the pressure could cause them to collapse.

After meticulously cleaning the molds and applying the release product, we carefully lay up our carbon fiber layers onto them. Next, we add the bleeder and breather materials before encasing the molds in vacuum bags.

Finally, the molds, along with the prepreg, will be placed in the autoclave to undergo the curing cycle. The process involves maintaining a temperature of 120 (°C) for 1 hour under a pressure of 4 (bars).

Thanks to the high quality of the molds and the additional pressure provided by the autoclave, we achieve a polished finish where the milling marks are imperceptible. The aim is to avoid manual labor on the molds to save time and costs.

4.5.1. Fuselage

For the manufacturing of the semi-monocoque, two molds will be necessary, one for the upper part and the other for the lower part.

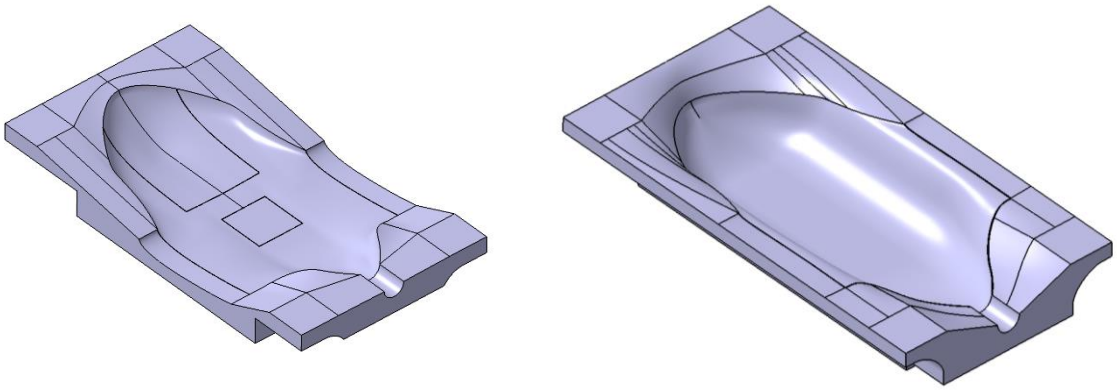

Figure 27. Fuselage molds

4.5.2. Wings

Five molds are needed to manufacture the wings. One for the upper camber surface of each side, one for the lower camber surface of the central half wing of both sides, and one for the lower camber surface of the external half wing of each side.

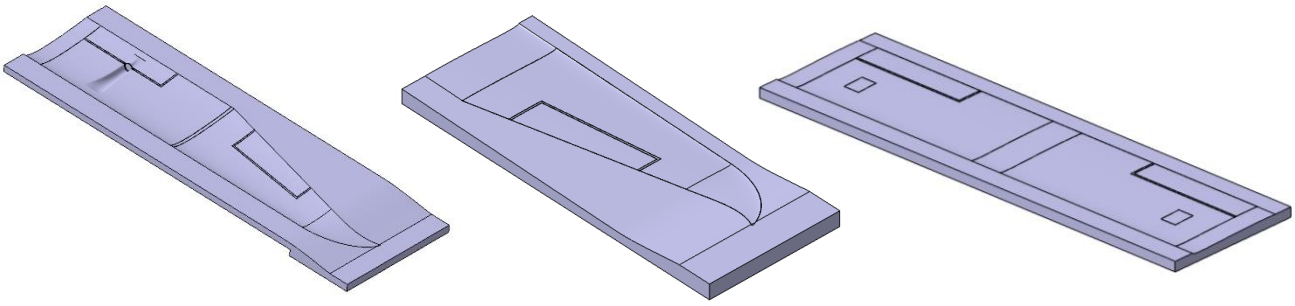

Figure 28. Wing molds

4.5.3. Empennage

For the manufacture of the empennage, two molds will be necessary, one for the lower camber surface and the other for the upper camber surface of the wing, since being in inverted V, the empennage, is symmetrical.

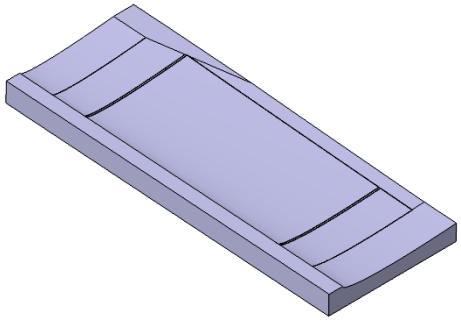

Figure 29. Empennage mold

To facilitate the cutting process, milling cutter marks have been used to delineate the areas where flight control surfaces are separated from the wing surface, and where the cap surface and telemetry's gap are separated from the fuselage surface. This helps to ensure precise cuts and proper alignment during assembly.

4.6. Landing gear design and positioning

Ultimately, it has been decided to opt for a tricycle configuration with commercially available landing gear and wheels, with proper positioning being essential to ensure the stability of the aircraft and the correct attainment of the estimated angle of attack for take-off, which in our case is 4º.

Regarding the chosen tricycle position: this configuration consists of a front wheel and two rear wheels, offering greater stability and control during take-off and landing. The front wheel helps to maintain the aircraft's nose in a controlled position, facilitating ground handling and avoiding the risk of excessive pitching during landing. Additionally, we have chosen an steerable nose landing gear to allow for better directional control both on the ground and during take-off and landing.

As for the choice of landing gear and wheels, our team has decided to procure them commercially. Some reasons for this decision include their durability and strength, as they are designed for repeated landings and varying terrain conditions; minimizing the risk of failures and providing better performance, as their optimized design offers superior performance in terms of weight, strength, and impact absorption capacity, contributing to a smoother and more controlled flight experience, as well as increased operational safety. Although compatibility and ease of installation of these components have been given greater importance, as commercial parts are typically designed to be compatible with a wide range of models and sizes, facilitating component selection and installation.

To facilitate selection and verification, our team has generated a database of commercial landing gear, placing great importance on suppliers and their reliability; that is, ease of contact with technical support and customer service.

Ultimately, by studying the stability of the aircraft, we have verified that using a commercially available 115 (mm) rear landing gear with a 60 (mm) diameter wheel and front landing gear with dimensions 158.5 (mm) height (including the wheel's diameter), at a distance of 280 (mm), the necessary 4º angle for take-off of our aircraft is achieved by attaching an extra 3D printed support for the nose landing gear.

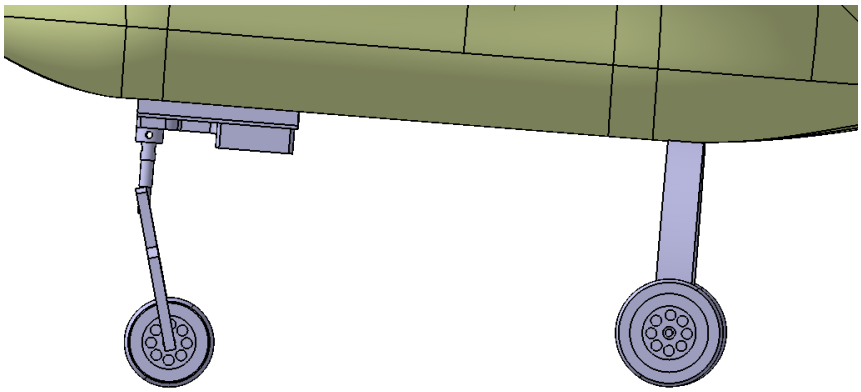

Figure 30. Landing gear

5.- Electronic Components

5.1. Electronic circuit and components

With regards to the aircraft's electronic circuit, to route the cables up to the wing control surfaces, rectangular perforations with rounded corners of 4.5x12 (mm) were made. These perforations are located at least 3 (mm) away from the adjacent spar, as this is a zone of high safety factor.

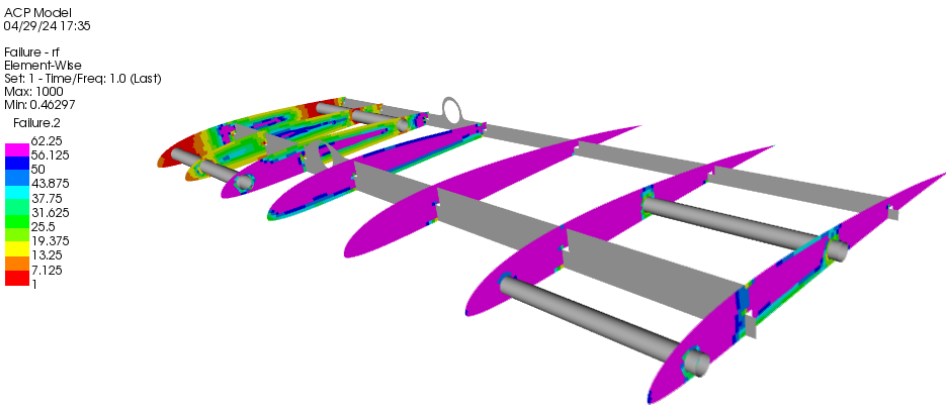

Figure 31. ACP simulation showing regions with the lowest demand for static loading.

Another important aspect is the wiring runs through the empennage tube. The tube had to be drilled for the cables to run inside it, with a 3D-printed piece attached at the other end. This piece also connects the tube that goes from the wing to the empennage.

The following diagram shows how the different components are connected to each other:

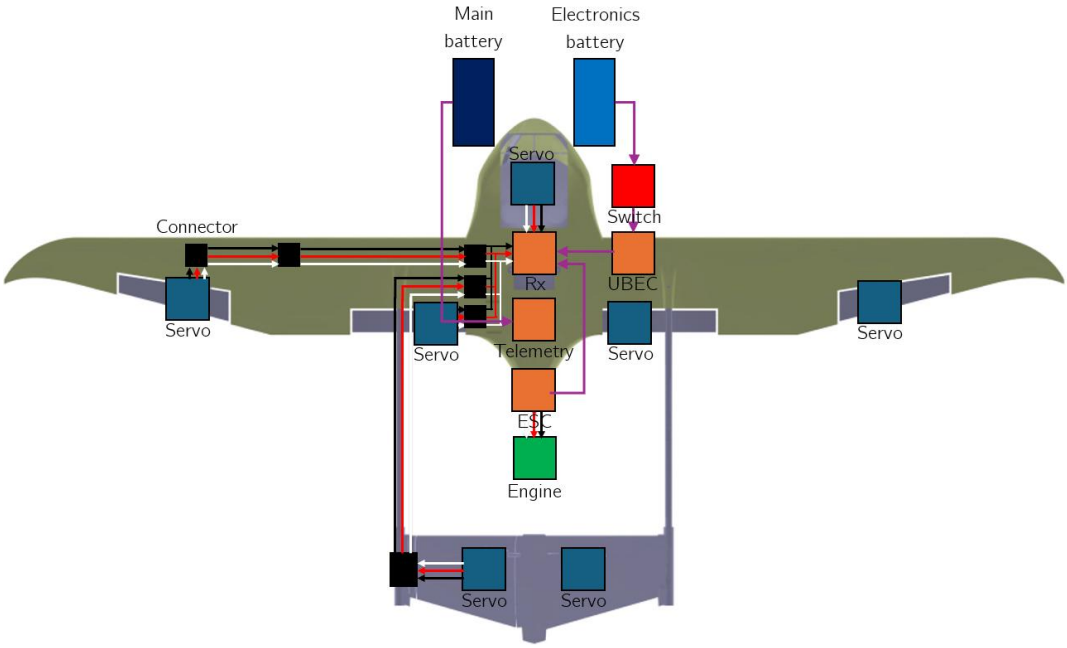

Figure 32. Component connections

5.2. Aileron mechanism

The main idea behind the aileron mechanism is to reduce drag as much as possible. Therefore, the rotary drive system (RDS) mechanism is ideal as it allows all the parts necessary to move the control surface to be cowled by the skin of the wing. The RDS mechanism consists of a twisted rib and a small 3D-printed housing for the rib and the hinge.

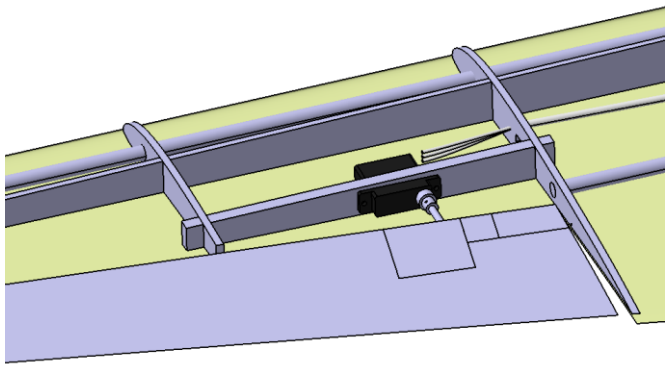

Figure 33. Aileron mechanism

5.3. Empennage system

The design of the empennage mechanism revolves around a configuration in which the servo rotates alongside the entirety of the empennage control surface. As a result of the mechanism being inside the carbon fiber skin, a significant drag reduction can be achieved.

The tail consists of a carbon fiber skin and a foam core. For this reason, it is required to design a cavity on the empennage foam core to, subsequently, generate it through machining and introduce all the components of the mechanism into the foam core.

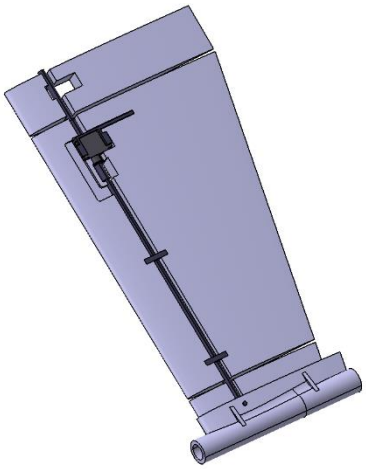

Figure 34. Empennage system

A 3D-printed piece serves as housing for the servo and to append it to the foam core. The servo's shaft is fastened to a tube that runs up until it locks to the fixed surface of the empennage. Hence, once the servo starts moving, the servo and the entirety of the empennage

control surface will rotate. This previously mentioned tube has two concentric supports attached to the surface. These supports serve as guides to mount the entire mechanism and are inserted into the mechanized foam core. However, not using bearings meant having to perform different tests to obtain the optimal tolerance between the tubes and their respective concentric contact surfaces. After that, the mechanism is lubricated to further reduce friction losses and maximize the servo's output torque. Finally, another tube is attached to the upper housing of the empennage to function as a hinge.

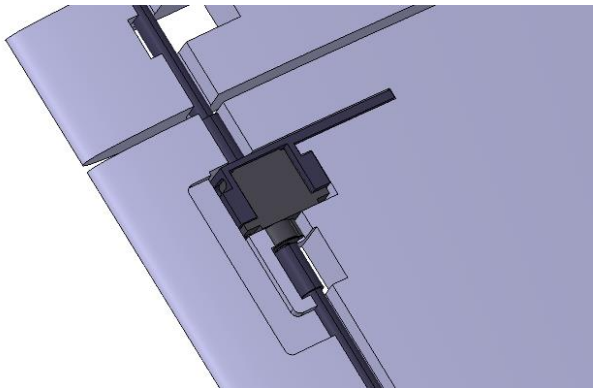

Figure 35. Empennage system zoom

The servo's cables are passed through a small opening on the 3D-printed housing piece. Afterwards, they are passed around a small gap on the foam to avoid clipping the moving parts, and then they get inserted into the main tube. This way, the relative rotation between the tube and the cables will be null, helping to maintain the integrity of said cables.

To assemble the tail, the core will be placed on the lower skin, after which the various parts that make up the mechanism will be introduced. To finish off, the mechanism will be closed with the upper skin.

5.4. Engine mount

When it comes to the engine mount, generative design helped find a topologically optimized solution. The resulting simulation is obtained from modelling the different loads that the engine mount would be subjected to during flight. Based on the results, areas where the factor of safety was higher than a certain value (usually >7) are emptied to reduce weight.

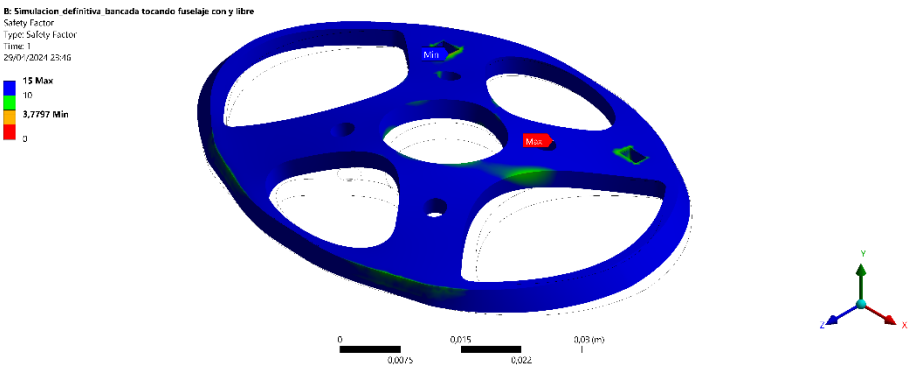

Figure 36. Engine mount

6.- Manufacturing

6.1. Laser cut

Both the carbon fiber and wood internal structures are cut using this method, giving us components with a dimensional tolerance of 0.1 (mm). This approach is not only swift but also highly efficient in material usage, granting us autonomy over the manufacturing process as we are not reliant on external companies or sponsors.

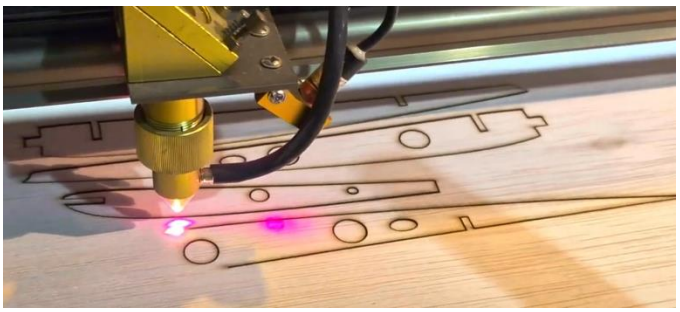

Figure 37. Laser cutting of ribs

6.2. 3D printing

3D printing is one of the most researched manufacturing processes in today's aeronautic context. It allows for the creation of optimized structures as well as opens the possibility to use many materials, from the more common polymers and plastics to state-of-the-art metal 3D or even composite printing.

A wide array of the aircraft components are manufactured using this process, mainly in PLA and LW-PLA, and some even in TPU. These components include the empennage joints, the cargo bay door, the landing gear assembly into the fuselage or the measurement box container.

6.3. Carbon fiber skins

The method used to manufacture the skins is hand layup since we use carbon fiber twill prepreg. The cut plies are laminated on the treated aluminum mould, then put inside a vacuum bag and sent to our sponsor, who cures it in the autoclave at 120 (ºC) and 4 (bar), to obtain a good surface quality.

6.4. Assembly

The assembly of all the components is done both by mechanical means, like intersecting spars and ribs, and with adhesive bonds, using epoxy, methacrylate, and cyanoacrylate. The internal structure is first assembled independently from the skin, after which the lower skin is bonded to it with adhesives. Electrical components are subsequently inserted and fixed into position, as well as the mechanisms and foam fillers. Finally, the upper skins are assembled to close the wings, fuselage, and empennage, resulting in all independent pieces being closed units to then be joined between them. Especially in the case of the fuselage, all important removable components are accessible from either the cargo bay or the measurement box opening.

7.- Payload Prediction

The specified payload for the competition consists of billiard balls weighing 157 (g) each. Considering the position of the cargo bay in the aircraft and with the aim of expediting the loading phase as much as possible, it has been decided that the maximum load capacity will be set at 7 balls.

To calculate the maximum payload our aircraft could transport during a flight under specific air density conditions on the runway, we have employed the equation for the most restrictive phase of the flight, which is the lift equation for take-off. Factoring the formula in air density and deducting the empty aircraft weight provides us a realistic approximation of the payload we can expect our aircraft to lift during the flight.

$$MPL(\rho) = MTOW(\rho) - OEW$$

$$MPL(\rho) = \frac{\frac{1}{2}\cdot V_{\infty}\cdot S\cdot C_{L\ TO}}{g}\cdot(\rho)\text{-}OEW$$

$$MPL(\rho) = 4.00458716\cdot(\rho)\text{-}2.745$$

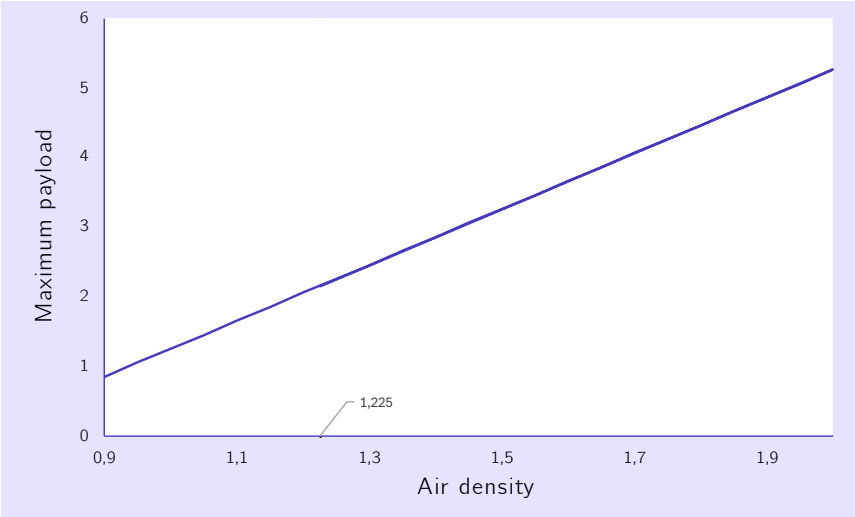

Table 4. Max. payload VS air density

8.- Outlook

We're currently wrapping up the final touches on some minor parts of the aircraft, such as small 3D printed components to seal the cargo bay and wing joints. These pieces are undergoing testing as we explore newly developed joining techniques, benefiting from valuable insights contributed by our new team members.

The carbon fiber manufacturing is currently on hold as we await the completion of the aluminum molds, which are expected to be finished by next week. Lamination and autoclave curing are scheduled to take place next month, with completion targeted before the start of June. Despite this timing setback due to sponsor-team coordination, we're confident that all laminates will be ready well in advance to allow for several test flights and even the assembly of another drone if necessary. Once the laminates are finished, the next step will be to assemble the entire aircraft. We're planning to work on both tasks simultaneously, with the internal structure assembly prepared to receive the skins once they are demoulded. This approach is deliberate to ensure that all dimensional restrictions between spars, stringers, and ribs are maintained, minimizing assembly errors. It's crucial for aerodynamic stability that the empennage tubes align precisely with the wings, avoiding any twisting or displacement.

The initial competition model will feature a wood internal structure and carbon fiber skins. Meanwhile, as this model is being prepared, the carbon fiber panels cured in the first cycles will be laser-cut to prepare a full-carbon fiber version. This approach aims to reduce weight compared to the wood version and achieve a goal the team has pursued since the last ACC: transitioning from an aluminum internal structure to a full composite one. In case laser cutting encounters difficulties, we are confident in the structural integrity of the wood design, validated through previous simulations. We will continue to explore alternative methods for crafting the carbon fiber structure, including water cutting or wire cutting, if necessary.

To familiarize our pilots with the aircraft we're assembling a 1:1 wooden model covered with Oracover skins, closely resembling the original drone. This model will serve as practice for assembling the definitive carbon fiber version. All components (servos, batteries, engine, landing gears, etc.) except for the structure and the flaps, will remain the same.

This way, the pilots have the chance to fly an aircraft with somewhat similar characteristics to the definitive model. It also makes it possible to test the take-off distance, carrying capacity and other such parameters, providing valuable insight on the accuracy of the tangible model when compared to the theoretical design. Additionally, these tests allow the pilots to feel ground behaviour, CG variability, gust response and other variables for when the carbon fiber plane is ready to be flown.

9.- Appendix

Marketing holds a vital role in any endeavor. Acknowledging the significance of projecting a robust and relatable team identity, we have undertaken a complete overhaul of our team's branding, encompassing aspects like the logo, color scheme, and typography.

Our team has developed a comprehensive marketing strategy that spans both digital and word-of-mouth marketing. In the realm of digital marketing, social media serves as a crucial tool for promoting our brand and for establishing close relationships with the community. We mainly leverage Instagram and LinkedIn for engagement. Additionally, our team's website (UVigo Aerotech - Aero Design Team | Web) serves as a central hub for accessing information and news about the team. Following our rebranding, we launched a modern, user-friendly website that facilitates seamless navigation and access to various sections covering news, events, projects, and social media channels. Notably, our bimonthly newsletter, accessible via the website, offers deeper insights into the team's activities, featuring updated design and content, including technical articles, interviews with team members, and information about our sponsors. Both the website and our social media platforms are experiencing.

Expanding our digital presence further, we've introduced a LinkedIn newsletter and have intensified our presence on TikTok and X, adopting a more aggressive marketing strategy. This approach leverages contemporary humor, similar to strategies employed by top companies, aiming to engage more effectively with our audience and expand our reach.

Regarding word-of-mouth marketing, since the beginning of this season, we have participated in engineering events and fairs at the provincial and regional levels. These events allow us to share our passion and expertise with fellow aeromodelling and engineering enthusiasts, effectively extending our team's commitment to design and manufacturing to a wider audience.

Moreover, the attire we don at these events and competitions serves a significant marketing tool. Each season, we design new hoodies and sponsor polos intended to make a strong impression on our audience. Our apparel not only acts as our introduction at both competitions and events but also ensures that the team is easily identifiable and recognizable, which is crucial for establishing a solid brand image.

9.1. Bibliography

[1] G. Benam, "XFLR5 Masterclass 3: ¿Cómo hago una aeronave estable? | Estabilidad estática y dinámica.," 2023.

[2] F.-A. e. Helmut Stettmaier, "V-Tails for Aeromodels," 1999.

[3] A. Deperrois, "Stability Analysis with XFLR5, A. Deperrois.," 2010.

[4] R. J. S. J. J. B. a. R. W. Steven A. Brandt, Introduction to Aeronautics: A Design Perspective, 1997.

[5] J. D. Anderson, Fundamentals of Aerodynamics, 1984.

[6] I. M. D. a. O. Ishai, Engineering Mechanics of Composite Materials, 1994.

[7] "Conceptual Design of Boom Mounted Inverted V-Tail in the Searcher MK".

[8] J. D. Anderson, Computational Fluid Dynamics: The Basics with Applications, 1995.

[9] K. K. Chawla, Composite Materials: Science and Engineering, 1987.

[10] D. P. MARTÍNEZ, "Anteproyecto de aeronave de ala fija," 2021.

[11] H. V. a. W. Malalasekera., An Introduction to Computational Fluid Dynamics: The Finite Volume Method, 1995.

[12] D. P. Raymer, Aircraft Design: A Conceptual Approach, 1989.

[13] B. W. McCormick, Aerodynamics, Aeronautics, and Flight Mechanics, 1979.

9.2. Illustrations

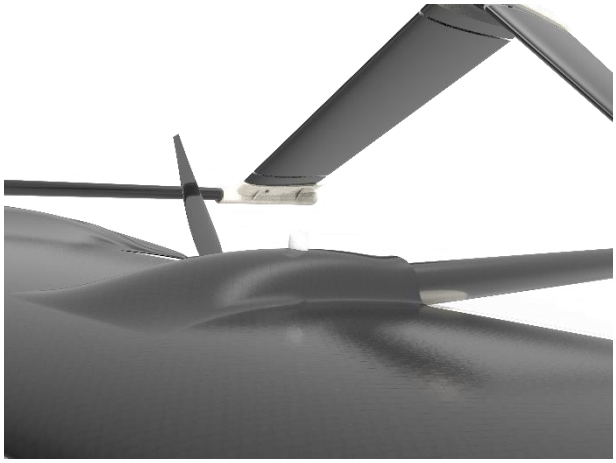

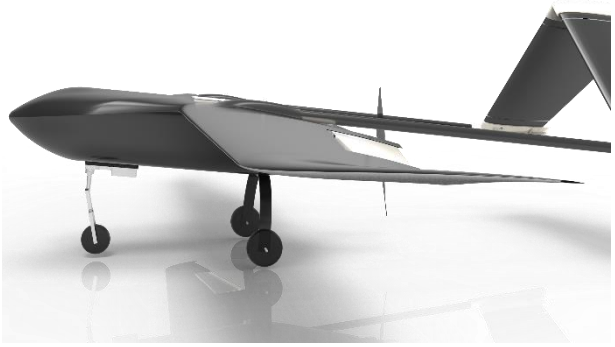

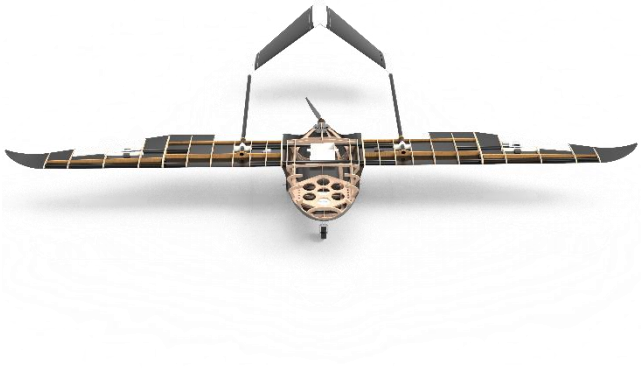

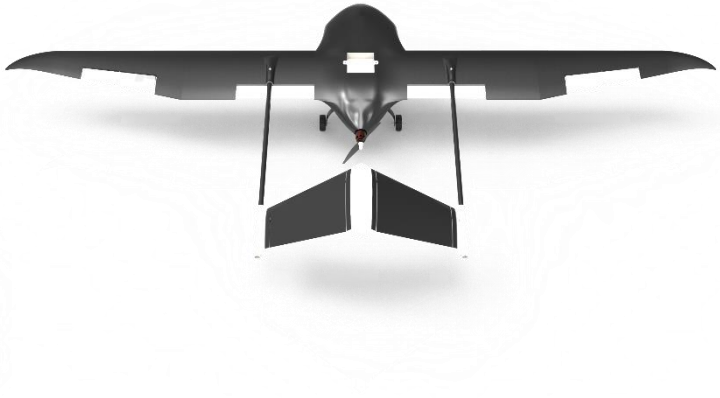

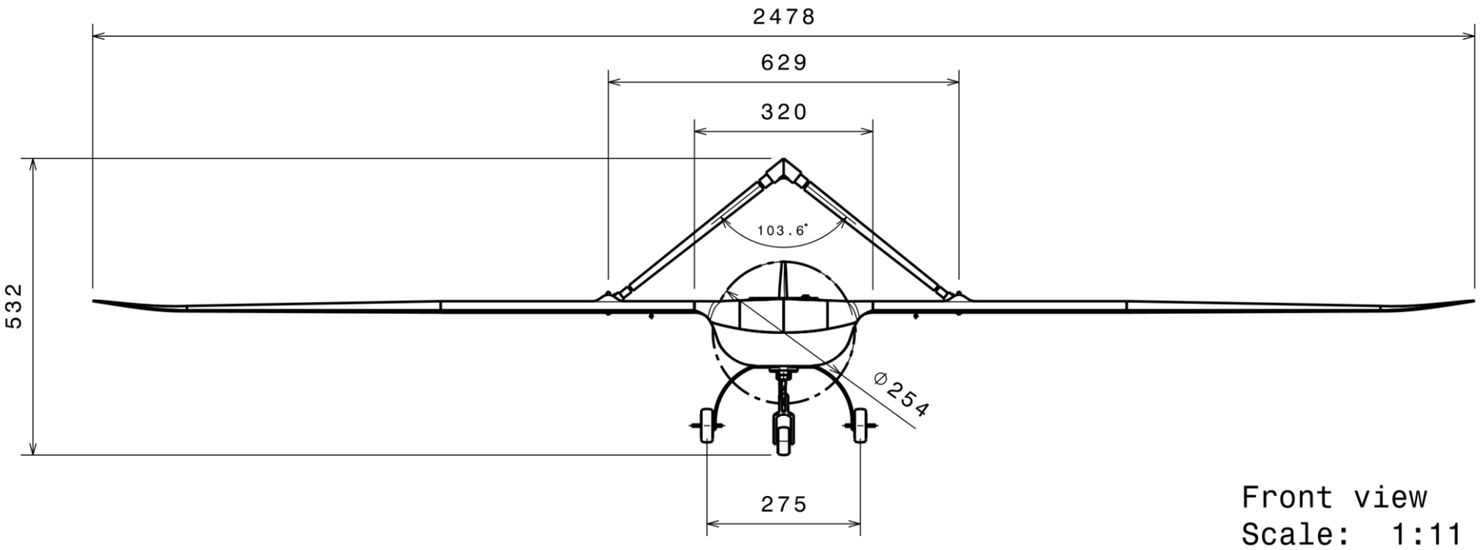

Front view
Scale: 1:11

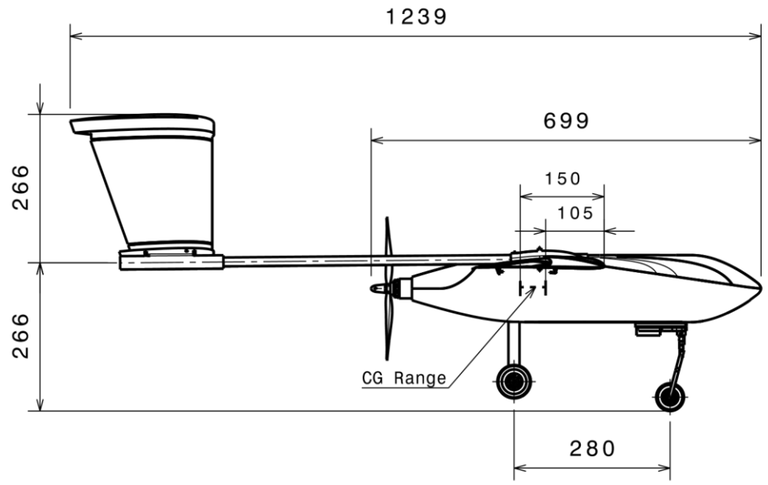

Starboard View
Scale: 1:11

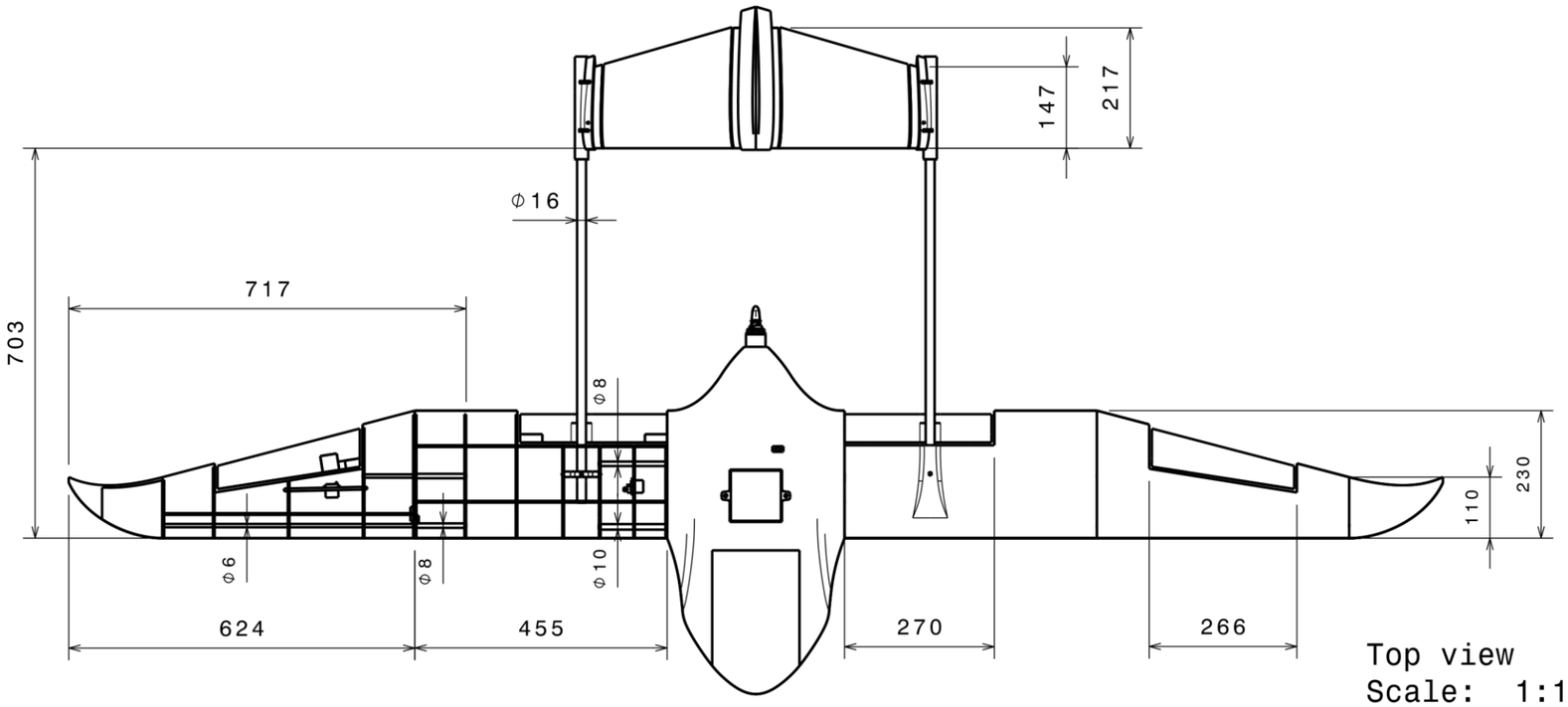

Top view
Scale: 1:11

UVIGO AEROTECH

Airfoil	Custom
Wing Area	0.36 m^2
Aspect Ratio	9.10
MTOW	4.9 Kg

Aircraft Designation: PROT. 1

Designed by
Uvigo Aerotech

Checked by
Uvigo Aerotech's Executive Board

SIZE	DRAWING NUMBER			
A3	01			
SCALE 1:11	MTOW(kg) 2.75Kg	MMSG	SHEET 1/4	

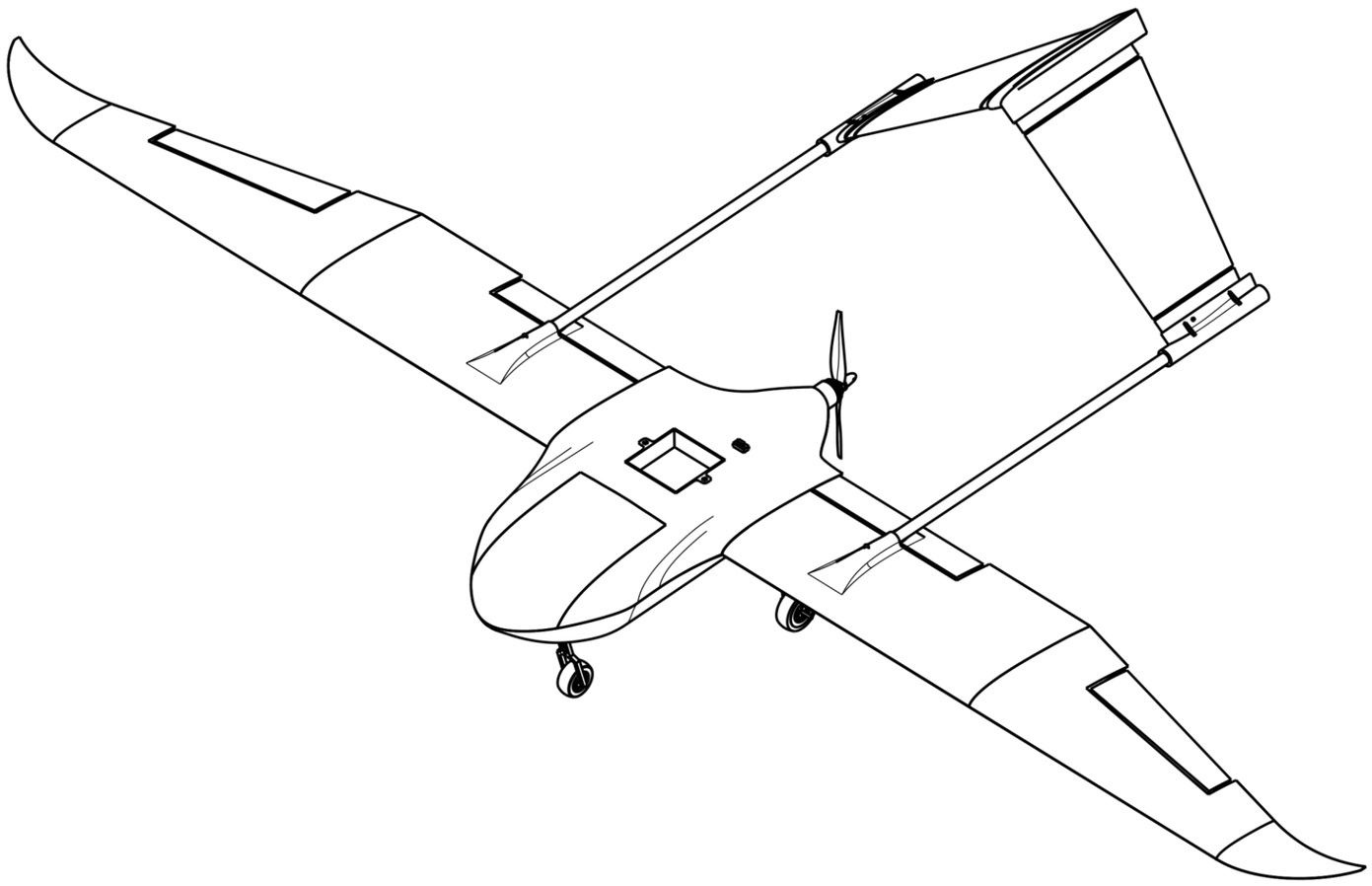

Isometric view
Scale: 1:8

Airfoil	Custom
Wing Area	0.36 m^2
Aspect Ratio	9.10
MTOW	4.9 Kg

Aircraft Designation: PROT. 1

Designed by Uvigo Aerotech	These drawings and design are property of UvigoAerotech and the University of Vigo. Created following ACC 2024 regulations.			
Checked by Uvigo Aerotech's Executive Board	SIZE A3	DRAWING NUMBER 02		
	SCALE 1:8	MTOW(kg) 2.75Kg	MMSG	SHEET 2/4

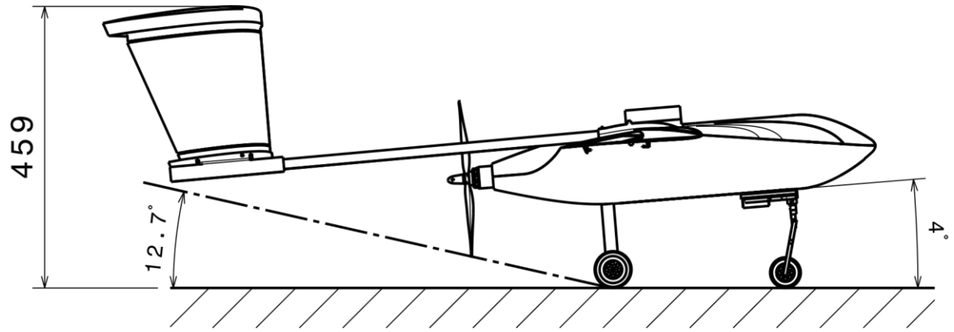

Ground Starboard View
Scale: 1:10

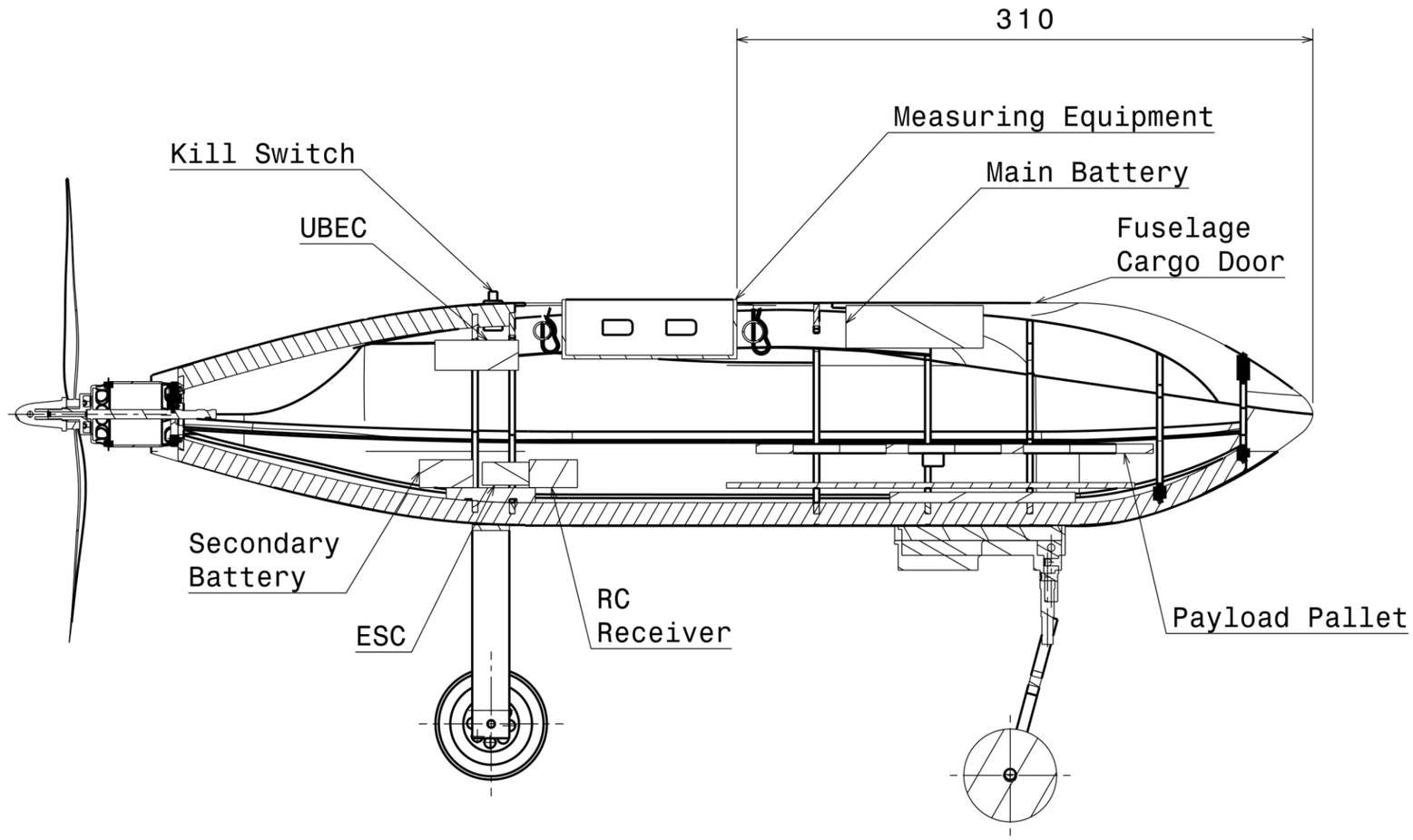

Section View
Scale: 1:3

UVIGO AEROTECH

Airfoil	Custom
Wing Area	0.36 m^2
Aspect Ratio	9.10
MTOW	4.9 Kg

Aircraft Designation: PROT. 1

Designed by
Uvigo Aerotech

Checked by
Uvigo Aerotech's Executive Board

SIZE A3 | DRAWING NUMBER 03

SCALE 1:11 | MTOW(kg) 2.75Kg | MMSG | SHEET 3/4

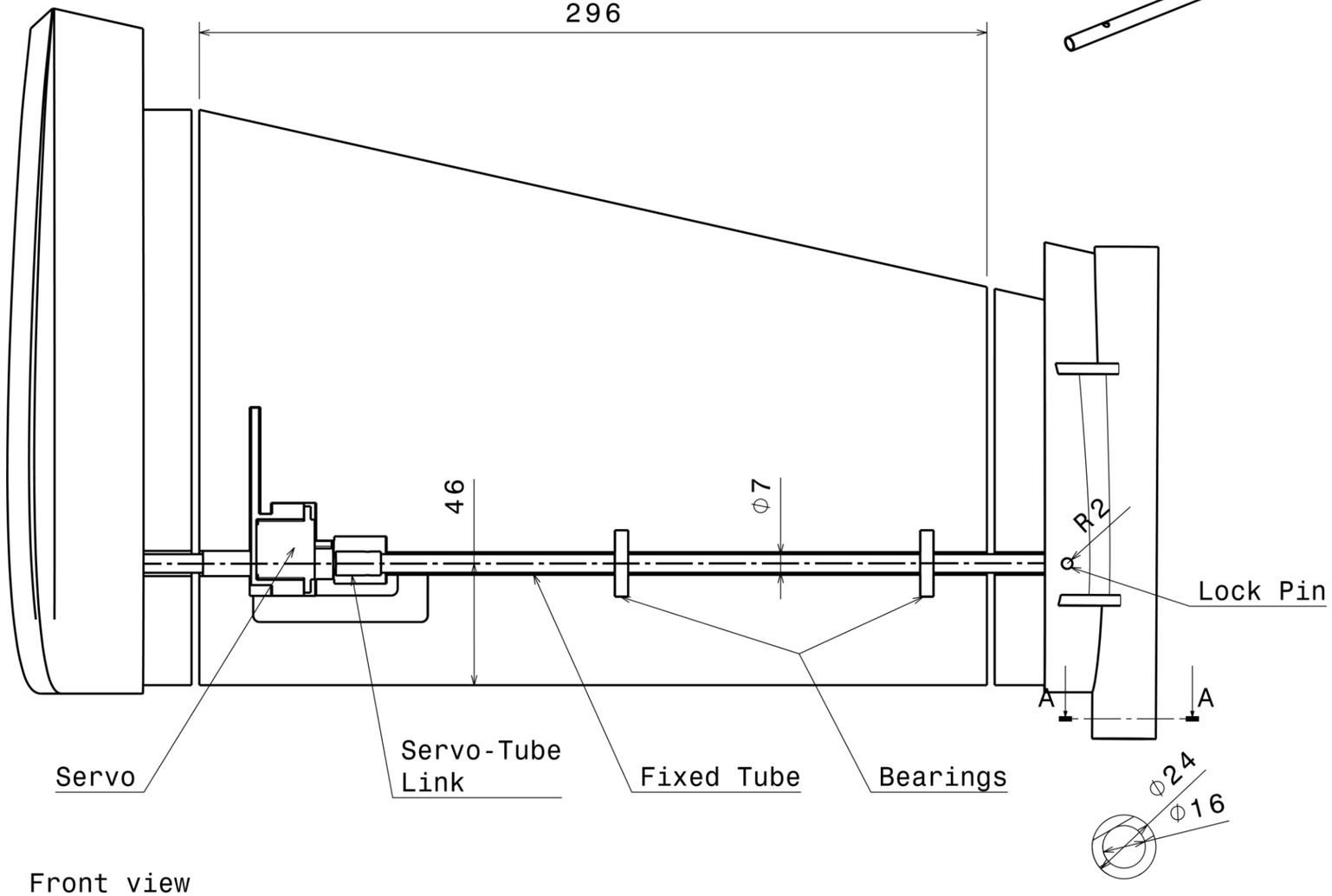

Front view
Scale: 1:2

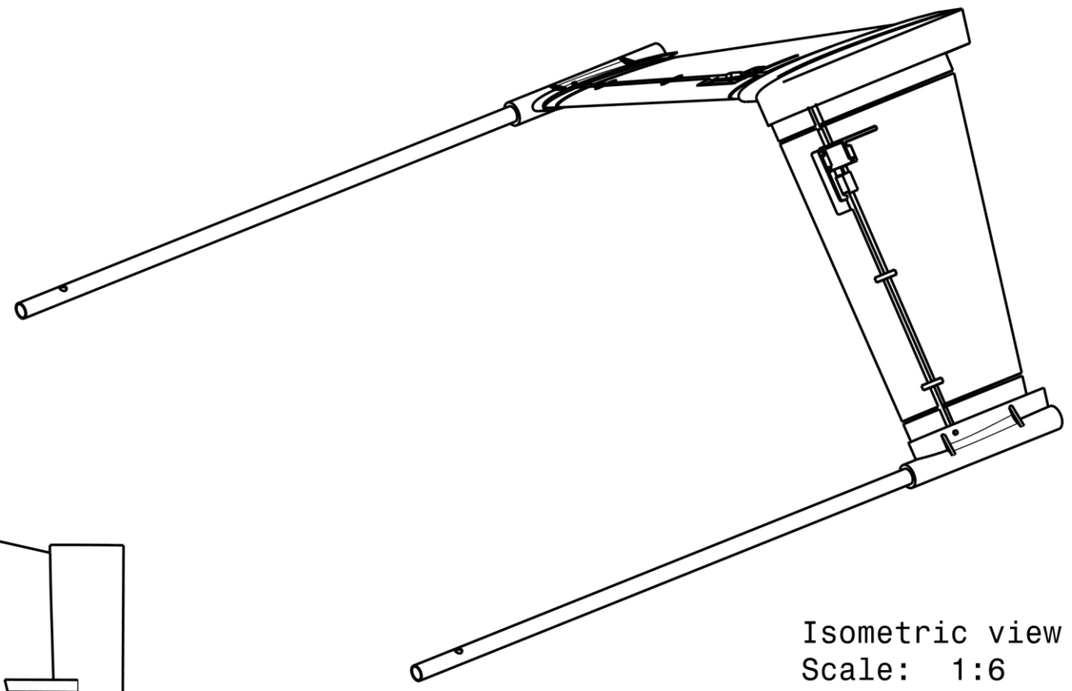

Isometric view
Scale: 1:6

UVIGO AEROTECH

Airfoil	Custom
Wing Area	0.36 m^2
Aspect Ratio	9.10
MTOW	4.9 Kg

Aircraft Designation: PROT. 1

Designed by
Uvigo Aerotech

Checked by
Uvigo Aerotech's Executive Board

SIZE A3 | DRAWING NUMBER 04

SCALE 1:11 | MTOW(kg) 2.75Kg | MMSG | SHEET 4/4